Title

MR-Compatible Haptic Display of Membrane Puncture in Robot-Assisted Needle Procedures.

Authors

Han, Amy
Bae, Jung
Gregoriou, Katerina
et al.

Publication Date

2018-03-19

DOI

10.1109/TOH.2018.2816074

Peer reviewed

HHS Public Access

Author manuscript

IEEE Trans Haptics. Author manuscript; available in PMC 2019 September 19.

MR-Compatible Haptic Display of Membrane Puncture in Robot-Assisted Needle Procedures

Amy Kyungwon Han[#] **[Student Member, IEEE]**,
Dept. of Mech. Engineering, Stanford University, Stanford, CA 94305, USA. kwhan@stanford.edu

Jung Hwa Bae[#] **[Student Member, IEEE]**,
Dept. of Mech. Engineering, Stanford University, Stanford, CA 94305, USA. jbae7@stanford.edu

Katerina C. Gregoriou [Student Member, IEEE],
Dept. of Mech. Engineering, Stanford University, Stanford, CA 94305, USA. kgrego@stanford.edu

Christopher J. Ploch [Student Member, IEEE],
Dept. of Mech. Engineering, Stanford University, Stanford, CA 94305, USA. cploch@stanford.edu

Roger E. Goldman,
Dept. of Radiology, Stanford University, Stanford, CA 94305, USA. goldmanr@stanford.edu, bdaniel@stanford.edu

Gary H. Glover,
Dept. of Electrical Engineering, Stanford University, Stanford, CA 94305, USA. gary.glover@stanford.edu

Bruce L. Daniel, and
Dept. of Radiology, Stanford University, Stanford, CA 94305, USA. goldmanr@stanford.edu, bdaniel@stanford.edu

Mark R. Cutkosky [Fellow, IEEE]
Dept. of Mech. Engineering, Stanford University, Stanford, CA 94305, USA. cutkosky@stanford.edu

[#] These authors contributed equally to this work.

Abstract

Multilayer electroactive polymer films actuate a small hand-held device to display tool tip forces during MR-guided interventions. The display produces localized skin stretch at the tips of the index finger and thumb. Tests confirm that the device does not significantly affect MR imaging and produces detectable stimuli in response to forces measured by a biopsy needle instrumented with fiber Bragg grating sensors. Tests with human subjects explored robotic and teleoperated paradigms to detect when the needle contacted a silicone membrane. The membrane was embedded in a tissue phantom that approximated the properties of porcine liver. In the robotic paradigm, naive users detected membranes with a 98.9% success rate as the needle was driven at fixed speed. In the teleoperated paradigm, users with experience in needle-based procedures controlled the needle insertion and detected membranes embedded in tissue phantoms with a 98.1 % success rate; some experienced users detected membranes with very light contact forces, but there was greater subject-to-subject variation.

Keywords

Haptic display; MR-compatible teleoperation; Medical robotics; Electro Active Polymer; Needle force display

1 Introduction

Magnetic resonance (MR) imaging has grown rapidly in popularity as a diagnostic tool, with an attendant interest in performing MR-guided procedures such as biopsy, cryotherapy, and brachytherapy [1], [2]. However, the narrow MR bore severely restricts patient access and manipulation space, requiring repeated removal and repositioning of patients during procedures. This prevents live imaging while operating and introduces patient shifting between scans, making image analysis difficult [1], [3]. To overcome these problems researchers have proposed robotic and teleoperated systems [4]–[9]. However, the majority of these systems isolate the physician from the tactile sensations of operating, such as inserting a needle through tissue of varying properties or puncturing a membrane.

One approach to restore haptic feedback is to create active or passive teleoperated systems that transmit forces from the tool tip to the operator [3], [10], [11]. A challenge in designing such systems is that any inertia, compliance, or friction will mask interaction forces. An additional challenge arises from the need to use MR-compatible materials and technologies. For example, the magnetic field precludes ferrous materials, and the apparatus must isolate and shield electronics with significant electrical currents [12], [13].

A low-power MR-compatible haptic display can address these difficulties by relaying tool-tip forces from contact with the patient to the fingertips of the operating physician (Fig. 1). In this paper we expand on results reported in [14] involving a biopsy needle instrumented with optical fibers to measure forces and a display using electroactive polymer (EAP) actuators to provide skin-stretch feedback at the fingertips. The current paper includes new test results to confirm MR-compatibility, a new human subject experiment, and a modified control approach to improve the lifetime of the actuators.

In the following sections we first review related prior work and then present the design and characterization of the EAP haptic display, including MR-compatibility testing. We then report on two experiments with human subjects. The first experiment explores detection of a membrane with the needle driven at fixed speed under computer control, providing a consistent force profile. The second experiment tests the device when the insertion speed is under direct human control, and accordingly varies. This condition would be expected in a teleoperated intervention. We conclude with a discussion of the user study results and recommendations for further work.

2 Related Work

Haptic displays have the potential to relay dynamic tool tip forces to the physician, compensating for the inertia, compliance, and friction that robotic and teleoperated systems introduce [15]–[17]. For example, haptic feedback has been explored for remote palpation

[18]–[20]. To restore the haptic feedback, a number of researchers present methods for reading forces on needles or catheters, some of which are MR-compatible [21]–[25]. Haptic feedback displays, like all systems used for MR-guided procedures, must use compatible materials and actuation technologies.

Various methods of actuation are possible for display. Ultrasonic piezoelectric motors can be designed with nonferromagnetic materials and low electric currents, which allow them to be MR-compatible [26]–[28]. However, they are inherently best suited as position-display devices as they are not backdrivable. Electrostatic motors are another admittance-type option [29]. Additional possibilities include pneumatic or cable-driven systems [4], [12], [30], [31], although these systems inevitably introduce some compliance and friction, especially if interaction forces must be transmitted through the entire system from slave to master. If electromagnetic motors are used, they require extensive shielding, even if located some distance from the bore [12]. Reviews on various MR-compatible actuators are available in [32], [33].

EAPs are lightweight, compliant, back-drivable and inherently MR-compatible with no metallic components and electrical currents on the order of microamps. Although they are compliant, they are more compact and light-weight than pneumatic and cable-driven solutions. This compliance does not substantially affect the overall dynamics of a robotic or teleoperated system if they are used only as small cutaneous displays at the user's fingertips. Other researchers have used EAPs for various haptic display applications including braille and wearable haptic interfaces [34], [35].

Additionally, EAPs have demonstrated feasibility for applications requiring MR-compatibility [36]–[38]. As actuators, EAPs have interesting properties in between those of ultrasonic motors and voice coil actuators: they are neither primarily displacement nor force sources. Rather, they are viscoelastic springs with varying force and stiffness as a function of the applied voltage. They can be matched to the requirements of a fingertip skin deformation display, which requires modest forces and moderate frequencies.

The system reported here involves skin deformation. Skin stretch and skin deformation displays are increasingly popular haptic modalities combining the ability to display direction and magnitude for both transient and sustained forces [39]–[43]. In the present case, we are interested in imparting lateral skin deformation at the tips of the index finger and thumb because these are the primary digits used in needle grasping.

3 EAP Haptic Device Design

As noted in sections 1 and 2, EAP actuators are good potential candidates for an MR-compatible skin deformation display. In this section we describe the design and fabrication of the EAP display used here.

3.1 EAP Mechanism

EAPs are dielectric elastomers covered with stretchable electrodes on the top and bottom surfaces. When a voltage is applied between the electrodes, the induced Maxwell stress

squeezes the dielectric elastomer, which subsequently expands in the planar directions. The Maxwell stress can be represented as [44]:

$$\sigma = \epsilon_0 \epsilon_r E = \epsilon (V/t)^2 \quad (1)$$

where ϵ_0 is the vacuum permittivity, ϵ_r is the relative permittivity, E is the applied electric field, V is the applied voltage, and t is the thickness.

In the present case, the elastomer is stretched over acrylic frames and approximately half of its area is covered with electrodes. The electrodes expand only in the $+x$ direction because the frames prevent motion in the y direction. The amount of motion in x is determined by the prestretch ratio (λ_1 by λ_2) of the film, as described in [14]. Fig. 2 (A) shows the EAP unpowered and (B) shows it actuated at 5.75 kV.

3.2 EAP Design and Fabrication

As with other EAP devices in the literature, we use 3M VHB 4910 acrylic film as the dielectric elastomer. It is first prestretched to 400% by 375% in the λ_1 and λ_2 directions respectively, as indicated in Fig. 2(B). As described in our previous paper [14], this prestretch ratio involves a tradeoff between displacement in the x direction and maximum force. The film and frame dimensions are 35 × 55 mm by 2.5 mm thick, including electrodes.

Masking patterns for the electrodes are laser-cut and placed on the stretched elastomer. Next, a thin layer of electrode is applied with a squeegee to the acrylic film. The electrodes are made with a mixture of soft silicone rubber (Smooth-On Inc., Dragon Skin 10 Fast), carbon particles (FuelCellStore, Vulcan XC 72R), and toluene, mixed with a weight ratio of 9:1:26, respectively, following an approach described in [45]. Connections to the electrodes are made with soft, conductive fiber tape. The area of the elastomer was monitored during stretching to maintain a consistent and uniform prestretch. However, there is inevitably some variability between samples because the fabrication was done by hand. Each EAP layer's performance differed by up to 5 %.

3.3 Device Layout

The primary design requirements are that the device be lightweight, compact, and able to produce displacements ranging from 0.05–1mm and forces from 0.1 – 2 N, values shown to be appropriate for lateral skin stretch [39]. We stack six layers of EAPs to achieve the desired force levels, giving a maximum of 1.6N at 5.5kV when motion is blocked. We use sand paper as the tactor covering to provide adequate friction with the finger pads and minimize slipping. The tactor is slightly recessed with respect to the surface of the device; this configuration grounds the skin at the periphery of the tactor window, a desirable property to maximize the skin deformation felt [46].

A modular design allows easy scaling of force as well as convenient repair of individual EAP layers. An insulating film is placed between EAP layers to prevent arcing between electrodes. An exploded view, dimensions, and weight of the device are shown in Fig. 3.

4 EAP Haptic Device Characterization

Tests were conducted to measure the force and displacement properties of the display as a function of applied voltage for a single EAP layer and for the multi-stack device described in Section 3.

4.1 Testing Setups

EAP force and displacement characterizations were performed with two setups: a muscle lever actuator (Aurora Scientific, 309C), and a load cell (ATI® Gamma), as shown in Fig. 4. Mathworks Simulink® was used to control the voltage output of a benchtop high voltage supply (TREK, 610B). To track the displacement, we recorded video of the EAP with a machinist's ruler in the video frame for reference. Four to five trials were undertaken in each case. The noise of the ATI is ± 0.03 N and for the muscle lever is ± 0.01 N. The displacement measurement resolution is 0.1 mm.

4.2 Performance with a Spring

To estimate the performance of the EAP when the tactor is in contact with a user's fingertip, a coil spring was connected to the EAP as shown in Fig. 4 (B). Its stiffness is 1.2N/mm, which is similar to that of a lightly loaded human fingerpad in the proximal-distal direction [39].

Although it is common to report the blocking force (zerodisplacement force) and free (unloaded) displacement of EAP actuators, we are primarily interested in the performance when connected to a load having approximately the stiffness of a human fingerpad. The blocked force and free-motion results of the display are reported in [14].

Fig. 5 shows the force-displacement performance for one, three and six layers of EAP film in the haptic device, connected to a 1.2N/mm spring, at voltages from 0 to 5.75kV. The voltage was reset to zero prior to each displacement test. Also shown are the corresponding displacements at 5.75 kV. The final design with six layers produces 0.85 N at 1.3 mm.

4.3 Force-Displacement Relationship

Although performance with a spring is a reasonable baseline, human fingerpad stiffness can vary considerably, in part as a function of gripping force [47]. To address this issue it is useful to measure the force-displacement behavior at a given voltage.

The force-displacement relationship for several voltages was found using a muscle lever as illustrated in Fig. 4 (A). First, to eliminate the viscous behavior of the EAP, it was charged for four seconds while held in place with the muscle lever at its undeflected position, as in Fig. 2 (A). The lever displacement then increased in increments of 0.1 or 0.2 mm, allowing the electrodes to expand. The corresponding force was measured at each position, resulting in the curves shown in Fig. 6.

To interpret the data in Fig. 6 it is useful to consider two different users. In this example, user (A) has a stiffer fingerpad than (B). This could be due to inherent properties like stiffness of the skin as well as controllable factors like tightness of the grip [47]. The EAP

actuator and the fingertip skin will move together, with the same displacement. The equilibrium point, where they come to rest, occurs when the forces are also equal – i.e., where the ascending (dashed) and descending (solid) lines intersect. Thus we see that user (A) will experience less displacement but a higher force than (B) for the same voltage. In summary, the perception of the stimulus depends on both force and displacement and we can estimate the force and displacement that a user experiences depending on their skin stiffness from Fig. 6. While the user studies presented in this paper do not have controllers that take individual skin stiffness into account, the variance of the absolute threshold test results (Section 7.1) provides enough information to create a haptic signal that is easily perceivable. Fully integrating the characterization results of Fig. 6 into a subject-specific closed-loop controller is a promising area of future work.

5 MR-Compatibility Tests

To use the haptic display for a robotic or teleoperated needle intervention under MR guidance, it is important to establish MR-compatibility. The standard requirements for MR-compatibility are (i) that the device should be safe to use in the high magnetic field and radio frequency waves from an MRI scanner, (ii) that the performance of the device should not significantly be affected by the MR field, and (iii) that the device should not reduce the quality of MR images. As the haptic device has no ferromagnetic materials and currents on the order of μA, it fulfills the requirement of safety in the MR environment. We also anticipate that it satisfies the remaining two requirements; to confirm this, we performed tests described in Sections 5.1 and 5.2.

The haptic device is designed to be part of a teleoperation system and thus placed outside of the MR bore. However, we also examined the more demanding case where a device is placed near the head coil for fMRI and we used the fMRI imaging sequence, which is more sensitive to disturbances in the magnetic field.

We also modified the high voltage (HV) circuit with respect to that used in [14] to reduce interference and improve the life expectancy of the EAP films. The modified circuit shown in Fig. 7 consolidates two optocoupler lines for compatibility with an existing data acquisition system in the MR facility and adds an inductor and capacitor to reduce noise. It also uses a miniature amplifier with low radio-frequency (RF) interference and a regulated current output. The small regulated HV DC to DC converter (EMCO X60, size 28 × 66 × 13 mm) amplifies an input signal ranging from 0 – 5 V, producing an output voltage from 0 – 6 k V. To actuate the device, the output of the converter is held at a constant high voltage and the optocouplers are used to charge and discharge the EAP devices. Two transistors turn the optocouplers on and off in accordance with a control line from the computer. A 1000:1 high voltage differential probe (Keysight Technologies Inc., N2891A) was used for testing the circuit. The DC power supply for the HV control circuit and computer were located outside the MR room. Wiring was passed through a standard filtered connector to the MR room to minimize RF noise from the computer and electrical system.

5.1 Effect of MR Field on Haptic Device Performance

To test the effect of the MR field on the performance of the device, the free displacement and the displacement when connected to a nonmagnetic spring of stiffness 1.37 N/mm were compared for conditions outside the MR room versus next to the head coil for a 3 T magnetic field (GE MR 750, Lucas center for imaging, Stanford).

The test results are shown in Fig. 8 and a Welch's t-test shows that there is no significant difference in free displacement (p-value: 0.08) or spring deflection (p-value: 0.6) when the EAP device is inside the MR bore and when it is outside of the MR room. Therefore, there is no significant effect of the high magnetic field.

To test performance, we first compare the force to that from Section 4.3. When the device was placed in series with a spring (1.37 N/mm), the EAP force was 0.69 N inside the MR bore and 0.72 N outside the MR room at 4.8 kV (derived from Fig. 8). These results fall within the range of scaled values from Fig. 6, which are 0.3 N (4 kV) and 0.76 N (5kV). Similarly, the free displacement measured at 4.8 kV is 1.1 mm inside the MR bore and 1.04 mm outside the MR room (Fig. 8), which falls in the predicted range derived from Fig. 6: 0.75 mm (4 kV) and 1.4 mm (5 kV).

Since the force and displacement test results do not differ significantly when the device is inside the MR bore and outside the MR room, and fall in the range predicted from Section 4.3, we can conclude that the performance of the haptic device was not significantly affected by the MR field.

5.2 Imaging Effects from Haptic Device

In this subsection we report on two test results of the imaging effects of the device and its miniature HV circuit in several configurations:

- **A** Baseline (everything off): miniature HV circuit and device inside the MRI room, 3 m away from the MR bore.
- **B** Located near an fMRI head coil (everything off): circuit located 3 m from bore, device located 14 cm from isocenter of the scanner.
- **C** HV circuit powered but no voltage sent to device; locations as in case B.
- **D** 3 kV square wave (50% duty cycle at 0.5 Hz) applied to device; locations as in case B.
- **E** 4.8 kV square wave (50% duty cycle at 0.5 Hz) applied to device; locations as in case B.

The first test analyzed the temporal signal/noise ratio (tSNR) for each of the cases (A-E). A 3 T GE MR 750 system and 8-channel head coil were again used to collect test data. The imaging target was a 175 mm diameter spherical agar phantom. An fMRI spiral-in/out imaging sequence was used with TR/TE/FA = 2000 ms/30 ms/90 deg and 3.43 × 3.43 × 0.4 mm voxel size. For the 3 T MR machine, the magnetic field strength falls below 10 Gauss (= 0.10 mT) at a distance of 3 m from the iso-center. The device was checked under both a very weak and a strong magnetic field (3 T) at a distance of 14 cm from the iso-center (the

distance from the iso-center to the end of the head coil). The results summarized in Table 1 show that there is not a significant decrease in tSNR when the device is activated.

The second test was performed using three plane images of the localizer scan and a Fast Gradient-recalled Echo imagine method with 31 kHz bandwidth. From the anatomic images acquired from the localizer scans of the phantom (Fig. 9) we observe that the standard deviation (SD) of background noise in the region of interest (ROI) is nearly the same for the baseline (case A) and when the EAP device was actuated with a 4.8 kV square wave (case E).

From the test results summarized in Table 1 and Fig. 9, we can conclude that there is not significant noise from operating in the MR field and that only minor image distortion was introduced by the haptic device.

6 Experimental System Setup

In this section, we describe the components of the user experiment setup. The apparatus combines a force sensing needle, a computer controlled linear stage, the haptic display, and tissue phantoms.

Fig. 10 shows the single-axis needle insertion system for the two user studies (robotic and teleoperated). The system consists of a passive linear rail (master side) that supports the haptic feedback device and a powered linear stage (slave side) operated under servo control by a microcontroller. The master side is instrumented with an encoder to capture motions imparted by the user and the slave side is equipped with a force sensing needle.

6.1 Force-Sensing Needle

A force-sensing needle, described in [23], provides force information for haptic display. It consists of an outer cannula (sheath) and an inner stylet that has three micromachined grooves, each containing an 80μm diameter optical fiber with four 3 mm long fiber Bragg gratings (FBGs) (DTG-LBL-1550 80μm FBGS International, Belgium) as shown in Fig. 11. The needle has a sharp trocar-tipped stylet and a blunt end tip cannula. The 18-gage needle is 15 cm long and the outer diameter of the cannula is 1.2 mm.

Fig. 12 shows typical force calibration data. The force resolution and the accuracy (RMS error) for these experiments was approximately 10 mN and 12 mN respectively after low-pass filtering (25 point moving average filter). Although friction acts along the entire outer cannula, the inner stylet is responsive primarily to forces at its exposed tip. For the user tests, C++ code runs at 1 kHz on a Linux computer to convert changes in optical wavelengths measured by the optical interrogator (Micron Optics, SM-130) to calibrated needle forces.

6.2 Tactile Feedback Rendering

After the FBG sensors are read and converted to force values and filtered, the corresponding voltage is computed for the high voltage amplifier in order to actuate the haptic display. Several strategies were used to minimize the effects of testing setup noise and slow EAP discharging.

Minimum force threshold: The force signals contain some noise due to inertial forces, friction between the needle tip and tissue, and temperature effects. Based on pilot force sensing, a threshold of 0.09 N (corresponding to 1.4 V input to the HV supply) is set for cleaner force rendering. As seen in Fig. 13, when the measured force is below this threshold, the HV amplifier input is fixed at 0.5 V, corresponding to the amplifier threshold voltage.

Discharging: Due to slow discharging of the EAPs, residual charge builds up if discharging is ended immediately after a sensed force spike. To prevent this, we program the HV amplifier to continually remain in discharging mode until the next force spike begins. This allows the EAP more time to fully discharge, ensuring greater fidelity to the force signal as shown in [14].

Maximum voltage: To prolong the life of the EAPs, the input voltage to the amplifier was capped at 3.3 V, corresponding to 4.5 kV output and ≈ 0.6 N force produced by the haptic device for a user with a fingertip stiffness of 1.2N/mm.

6.3 Needle Insertion System

The master and slave sides of the needle insertion system are mechanically isolated and coupled by an electronic control system. The slave system is a single-axis linear stage (MAXY4009W2-S4–0, Velmex Inc.) that supports the needle as it is driven into a tissue phantom under position control (Fig. 14B). The positioning accuracy of the motor control loop is approximately 60 μm with speeds of up to 11 mm/s. In the robotic paradigm, the slave side inserts the needle automatically at a constant speed regardless of the position of the master side, and the user stops the motion by pressing a button. In the teleoperated test, the slave side follows the master side's position, and is thus directly controlled by the user. This single-axis needle insertion system is a proxy for an eventual MR-compatible robotic or teleoperated system.

6.4 Tissue Phantom with Embedded Membrane

The tissue phantom material for both the robotic and teleoperated user studies was the same; however, the membrane type and location differed. Tissue phantoms were made of gelatin (Knox Unflavored Gelatin) with a ratio of gelatin powder to water of 1:4. The stiffness of the gelatin was 8.3 kPa, which is in the range of the Young's modulus for normal and fibrotic liver [48]. The membrane used for the robotic user study has a 1.01 N (SD = 0.01 N) puncture force required to penetrate the plastic film membrane, 12.5 μm thick. A membrane was located at a different depth from the top surface: 3 cm, 6 cm, or 8 cm for each of 3 phantoms. The phantoms were used 6 times each in random order, resulting in 18 insertion tests. Phantoms were covered with a curtain to prevent participants from receiving visual feedback.

In the teleoperated study, the membrane consisted of a wipe (Kimwipes) coated with a layer of silicone (Dragon Skin Fx-Pro) with a total thickness of 0.6 mm [3], [49]. The thickness and material were determined empirically, by comparison to the puncture force of an ex-vivo porcine liver outer membrane, which is approximately 0.17N (SD = 0.06N) with a constant insertion speed of 6 mm/s. The ex-vivo porcine liver outer membrane was separated from the

rest of the liver tissue using a sharp razor blade. To measure the puncture force, both the artificial and porcine membranes were mounted in a rectangular frame and punctured using the instrumented needle described in Section 6.1. Fig. 15 shows similar peak amplitudes for the two membranes. The phantoms were 8 × 8 cm in cross-section and 7 cm in depth, allowing multiple needle insertions. Membrane puncture forces measured were similar for multiple punctures across the area as long as the gap between insertions was larger than 5 mm. In each phantom a membrane was embedded at 2.5 cm from the top surface, as seen in Fig. 14 C.

7 User Studies

To help in interpreting the subsequent user tests, we begin with a brief summary of psychophysical test results from a previous paper [14]. All user experiments were conducted under Stanford University IRB protocol 26526.

7.1 Absolute Displacement Threshold Test

Twelve test subjects (10 male, 2 female, age range: 23–33 years old, mean age: 26.1 years old), all without medical experience in manipulating needles, were recruited for the first experiment. We trained the subjects to maintain a similar grip force for the experiments.

To test the functionality of the EAP skin stretch device, we first checked the absolute threshold for users to detect displacement, and compared it to other skin stretch devices that use small RC servos or DC motors. A simple up-down staircase method was used to obtain the detection threshold (X_{50}) [50]. The initial stimulus magnitude was chosen based on a pilot study, and was found to settle within the chosen number of reversals. Data were collected until the 12th reversal, and analyzed as described in [50]. Stimuli were given at random intervals to prevent users from predicting the timing. In operation, the skin stretch device's tactors moved with a predefined speed until they reached the target stimulus magnitude. They then dwelled for 2 seconds and returned to the initial position at 1/6 the speed. Thresholds were obtained for 0.25 N/s, 0.52 N/s, and 1.06 N/s. In all cases, the initial stimulus was 0.12 N.

The results summarized in Table 2 are consistent with prior research on skin stretch displays (e.g., [39], [40]), which report an absolute threshold that decreases as the speed of displacement increases.

7.2 Robotic Membrane Detection

The robotic membrane detection test is described in more detail in [14] and summarized here briefly for comparison with the teleoperated paradigm in the next section. In the robotic test the needle was driven at a constant 6 mm/s into a tissue phantom with a membrane at a variable depth.

Users were told to move the EAP device on a rail (Fig. 10) while holding the tactors, approximately following the predefined motion of the needle. In this scenario, the users are passive observers of the haptic stimuli and are asked to press a button when they feel a stimulus corresponding to membrane contact. The users (N = 10) were the same as in the

threshold test in the previous section (7.1) and were trained through two example membrane punctures.

Successful membrane detection was defined as the user stopping the linear stage shortly after the needle contacted the membrane. The distance between the membrane and needle tip was measured with an encoder on the linear stage.

7.2.1 Results—Users (N = 10) successfully detected 98.9% of membranes over a total of 180 trials, with the needle stopping an average distance of 4.5 mm past the membrane (SD= 1.6 mm). Most of this distance was due to communication delays and inertia of the linear stage.

First, there is approximately 50 ms delay between the input signal and the start of EAP actuation. With the linear stage moving at 6 mm/s, the force ramps up at approximately 0.6 N/s. Given the threshold detection results, this corresponds to 117±17 ms to reach the threshold force. Next is the reaction time of a user to press a switch, which has been reported as 367ms [51] or as 325 ±84 ms [52]. The last step is the mechanical time constant of the stage, which requires approximately 333 ms after the button press to come to a complete stop. Thus, in total, approximately 850 ms of time delay may occur between membrane contact and needle stoppage.

This time delay corresponds to a 5.1 mm displacement of the stage. Since our measured result of 4.5 mm (SD =1.6 mm) is comparable with the above calculation, we can conclude that the membrane puncture was detected successfully and promptly.

7.3 Teleoperated Membrane Detection

A second study explored a teleoperated scenario with users experienced in needle-based procedures. The subjects for the second study were individuals in the Stanford University Deptartment of Radiology with 1 to 30 years of experience in needle-based procedures. We tested 10 users but excluded one user’s data due to a misinterpretation of the study’s directions, leaving a total of 9 users.

In this scenario, users control the motion of the needle by pushing the haptic device along its linear rail. A microcontroller servos the linear stage to match the user’s measured velocity, which may vary.

Needle tip forces are relayed via the haptic feedback device while the force sensing needle is inserted into the tissue phantoms described in Section 6.4. In this test, users were asked to stop moving the master when they detected that the needle tip had contacted a membrane within the tissue phantom.

7.3.1 User Training—We first familiarized the subjects with the skin stretch stimulus. Users placed their fingers on the two tactors of the EAP haptic device without moving along the linear rail. We then applied signals at random intervals to confirm that they could detect the stimulus.

To provide a sense of the tactile feedback of membrane puncture, we trained users as in the robotic paradigm to detect haptic stimuli as the needle was driven at a fixed speed of 2, 4, or 6 mm/s. We asked subjects to approximately follow the motion of the needle by pushing the haptic display along its linear rail (master side) and to respond to the haptic stimulus when they detected a membrane. The motivation for testing at three speeds is that the puncturing force increases faster at higher insertion speeds [53], and the sensitivity to skin stretch also increases with speed [39], [40].

7.3.2 Experiment Procedure—We used a gelatin tissue phantom with a membrane located 2.5 cm from the top surface (described in Section 6.4). However, we started each test with the needle inserted a randomized distance of 0.5, 1, or 1.5 cm inside the phantom.

We asked users to push the master at a user-determined approximately constant speed (i.e., no sudden acceleration or deceleration) in the range of 2 – 6 mm/s. Users were asked to stop the motion as soon as they felt a haptic stimulus corresponding to the tip of the needle contacting the membrane.

7.3.3 Results—Users (N = 9) were able to detect the membrane successfully in 105 of 107 insertions (98.1% success rate). In 14 out of 105 successful membrane detections, users stopped the needle fast enough not to puncture the membrane. In the remaining 91 insertions, users successfully detected and punctured the membrane while decelerating the haptic device on the linear rail.

The needle fully stopped after 2.78 mm (SD = 1.66 mm) from the initial contact of the membrane. This distance includes the stretch of the membrane (2.44 mm, SD = 1.72 mm) and the distance the needle traveled after puncturing the membrane (0.34 mm, SD = 0.46 mm). The results are summarized in Table 3.

To interpret the data it is useful to realize that membrane puncture can occur in two different ways. In the first case, illustrated in Fig. 16(A), both the stylet and the outer cannula pass through the membrane with a corresponding rapid drop in the force. This produces a strong transient signal for the haptic device. In the second case, shown in Fig. 16(B), only the stylet pierces the membrane. The force remains roughly constant after increasing. Note that this sustained force will continue to be rendered by the haptic device and, because skin stretch stimulates slow-adapting as well as fast-adapting mechanoreceptors [54], [55], it will continue to provide a sensible stimulus to the user.

Compared to the robotic membrane detection test, users operated the needle at various insertion speeds, with an average of 5.46 mm/s (SD = 2.65 mm/s). The average membrane puncture force of 0.19 N (SD = 0.05N) is slightly higher than the force (0.17 N) measured with a constant insertion speed of 6 mm/s. This average force corresponds to 2.9 V control input voltage to the HV circuit, producing 0.5 N at the haptic device when actuated against a 1.2N/mm spring.

To further interpret the results, we consider that needle insertion speed affects the peak force of a membrane puncture [53]. Accordingly, we are interested in whether the measured peak force varies with the needle insertion speed. In addition, we consider the correlations

between insertion speed and the rate of change in the control input voltage of the HV circuit, as well as the distance the needle travels after contacting the membrane.

As seen in Fig. 17, peak axial force from the needle increases with insertion speed, which is consistent with previously reported results. Within the small displacement range, the peak force is larger for faster insertion speeds because the corresponding force also increases more rapidly [53]. Perhaps not surprisingly, the stopping distance also increases with insertion speed, although the correlation is less strong. This is despite the fact that the commanded voltage to the haptic display and the haptic stimulus intensity also increase with insertion speed.

To interpret the data on stopping distance it is again useful to consider the effect of delays in the system. As in the robotic test, there is a 50 ms latency between a force measured at the needle tip and a high voltage command to the haptic display. In addition, there may be ≈ 300 ms human reaction time, although the response may be faster when the stimulus occurs as a direct result of human motion. For an average insertion speed of 5.65 mm/s (SD = 2.65 mm/s), these delays suggest that the needle will stop approximately 2.4mm past the membrane. Adding the membrane thickness, 0.6 mm to 2.4 mm, we estimate a detection-stop distance of 3 mm. This estimate aligns with our measured detection-stop distance of 2.8 mm.

8 User Studies Discussion

The results of the robotic test with naive users and the teleoperated test with users experienced in needle procedures are similar. In both cases the detection rate is very high (≈ 98%), indicating that users had no difficulty in detecting the stimulus.

The stopping distance, after accounting for communication latency and inertia in the system, is also similar (slightly under 3 mm). This result is perhaps less expected given the differences in conditions between the two experiments.

In the first experiment, users were responding to an autonomously driven needle, receiving a haptic “event cue” that was anticipated but after an uncertain interval. They had no difficulty recognizing the cue and pressing a button, with typical human response times. In the second experiment, users received the haptic stimulus as part of an afferent/efferent loop. Moreover, these were users with experience in manipulating needles and detecting the forces associated with contacting membranes. Indeed, a few of the experienced users did produce very low average forces (0.14 N in one case) and were able to detect the membrane without ever piercing it.

However, in the second experiment, users were free to chose their own preferred speed to guide the needle via the master device. They also applied more or less side load on the sliding rail, which could produce slightly more friction. Finally, in the second experiment, users stopped the needle by arresting the motion of a (slowly) moving hand, which is not the same as pressing a button. Given that the puncture force and the rate of ramp-up of the displayed force both depend on speed, it is not surprising that there was more subject-to-subject variability. One additional difference is that the phantom and membrane were

somewhat different in the second experiment; in particular, the membrane could stretch up to 2.44 mm before puncture.

We also observed two instances in the second test where users failed to detect the membrane contact event. The failure occurred during the corresponding user's first trial. The peak force, insertion speed, and force slope did not differ significantly from successful membrane detections. We speculate that the two cases of detection failure were caused by the initial learning curve associated with using a new device and could be remedied with additional training.

9 Conclusion and Future Work

We present a new MR-compatible haptic display that functions by eliciting skin stretch in the proximal/distal direction when a user holds it between the thumb and index finger. The device is intended to display forces sensed at the tip of a tool, such as an instrumented biopsy needle, during MR-guided interventions. Tests in a 3 T MR machine confirm that the device and its high voltage power supply do not significantly affect the signal/noise ratio of the MR image, even located near the head coil in an fMRI application; neither is performance of the device affected by the magnetic field.

We additionally present the results of two sets of user experiments. In the first case, users were asked to respond to the haptic stimulus they received as an instrumented needle was driven at fixed speed through a tissue phantom and into a plastic membrane. Users were able to respond reliably and accurately, arresting needle motion by pressing a button. In the second test, we recruited users with experience in needle manipulation to perform a single-axis teleoperated needle insertion. Users guided a master along a low-friction rail and received haptic stimuli from the device. A slave axis moved the needle through the phantom. Users were again able to detect membrane contact with very high reliability, although there was somewhat more subject-to-subject variability as users chose different speeds to propel the needle.

The results of these tests suggest that a haptic display that imparts lateral skin stretch using electroactive polymer actuators is a good candidate for MR-guided robotic and teleoperated interventions. It has the potential to provide physicians with an unprecedented capability: the ability to sense remote forces as though one's fingertips were located remotely at the tip of a tool inside the MR machine.

Extensions to the work will include integrating the display into a complete MR-compatible teleoperated system. Interestingly, given that skin stretch (unlike vibrational feedback) is inherently directional and can display static as well as dynamic forces, there is the ability to provide a multiaxis skin stretch feedback, perhaps using mechanisms such as those presented in other work [41].

Acknowledgments

The corresponding authors are A.K. Han and J.H. Bae. A.K. Han is supported by a Samsung Scholarship, J.H. Bae is supported by the Kwanjeong Educational Fellowship, and C.J. Ploch is partially supported by affiliate funding from Stanford Center for Design Research. G.H. Glover is supported by NIH P41 EB0015891. Additional support

was provided by NIH PO1 CA159992 and NIH SBIR R43-EB011822 and by NSF CHS 1617122. User tests were conducted under Protocol IRB-26526. The authors thank Dr. Debra Ikeda for help in arranging the user study at Stanford Hospital, and Dr. Jeremy Heit and Dr. Michael Iv for discussion of possible applications of the technology.

Biography

Amy Kyungwon Han received the M.S. degree from Stanford University (2015) and the B.S. degree from Georgia Tech (2012) in Mechanical Engineering. She is currently a Ph.D candidate in Mechanical Engineering at Stanford University. Her research interests include bioinspired robots, soft actuators, electroactive polymers, and haptics.

Jung Hwa Bae received the B.S. degree in mechanical engineering in 2011 from Korea Advanced Institute of Science and Technology (KAIST), Daejeon, South Korea and the M.S. degree in mechanical engineering in 2013 from Stanford University, Stanford, CA, where she is currently completing a Ph.D. in mechanical engineering. Her research interests include the design and development of force sensors and haptic devices for medical, automotive, and augmented reality applications.

Katerina C. Gregoriou is an undergraduate student in Mechanical Engineering, with a minor in Human Biology, at Stanford University. Her work focuses on haptic applications of medical devices, including a collaboration with Cardiovascular Medicine at the Stanford School of Medicine. Her interests include rehabilitation robotics, materials science applications in medical devices, and human factors in design. She is a student member of IEEE, IEEE Women in Engineering, and IEEE SIGHT.

Christopher J. Ploch received the B.S. degree in engineering in 2010 from Hope College and the M.S. degree in mechanical engineering in 2012 from Stanford University. He is currently a Ph.D. candidate in mechanical engineering. His research interests include the design and control of haptic devices and robotic systems for applications in driving, medical devices, and virtual reality.

Roger E. Goldman received the B.Sc. degree in mechanical engineering from Stanford University, Stanford, CA, USA, in 2002 and the Ph.D. degree in biomedical engineering and the M.D. degree from Columbia University, New York, NY, USA, in 2012 and 2013, respectively. He is currently a diagnostic radiology resident in the Department of Radiology, Stanford University.

Gary H. Glover received the Ph.D. in Electrical Engineering from U. Minn. in 1969. He joined GEs Corporate R&D Labs in Schenectady until 1976, and moved to GE Medical Systems in Milwaukee to help transition fan-beam CT technology. He was instrumental in defining CT and MR products for GE. He joined Stanfords Radiology Dept. as Professor in 1990. His research includes MRI physics and fMRI. His students' contributions include techniques for acquisition and analysis of fMRI data and multimodal neu-roimaging.

Bruce L. Daniel received the MD degree from Harvard Medical School in 1990. He is Professor of Radiology at Stanford University. His research interests include magnetic resonance imaging (MRI) of the body and breast, MR-guided procedures, and mixed-reality medicine. He is a Distinguished Investigator of the Academy of Radiology Research, a Fellow of the American Institute for Medical and Biological Engineering, and a Fellow of the Society for Computed Body Tomography and Magnetic Resonance.

Mark R. Cutkosky received the Ph.D. degree in mechanical engineering from Carnegie Mellon University, Pittburgh, PA, USA, in 1985. He is the Fletcher Jones Professor in mechanical engineering at Stanford University, Stanford, CA, USA. His research interests include bioinspired robots, haptics and rapid prototyping processes. Dr. Cutkosky is a Fellow of the ASME and IEEE.

References

[1]. Smith-Bindman R, Miglioretti DL, Johnson E, Lee C, Feigelson HS, Flynn M, Greenlee RT, Kruger RL, Hornbrook MC, Roblin D et al., "Use of diagnostic imaging studies and associated radiation exposure for patients enrolled in large integrated health care systems, 1996–2010," Jama, vol. 307, no. 22, pp. 2400–2409, 2012. [PubMed: 22692172]

[2]. Tsekos NV, Khanicheh A, Christoforou E, and Mavroidis C, "Magnetic resonance-compatible robotic and mechatronics systems for image-guided interventions and rehabilitation: a review study." Annual Review of Biomedical Engineering, vol. 9, no. 1, pp. 351–387, 2007.

[3]. Burkhard N, Frishman S, Gruebele A, Whitney JP, Goldman R, Daniel B, and Cutkosky M, "A rolling-diaphragm hydrostatic transmission for remote MR-guided needle insertion," in Robotics and Automation (ICRA), 2017 IEEE International Conference on. IEEE, 2017, pp. 1148–1153.

[4]. Gassert R, Moser R, Burdet E, and Bleuler H, "MRI/fMRI-compatible robotic system with force feedback for interaction with human motion," IEEE/ASME Transactions on Mechatronics, vol. 11, no. 2, pp. 216–224, 2006.

[5]. Macura KJ and Stoianovici D, "Advancements in magnetic resonance-guided robotic interventions in the prostate," Topics in Magnetic Resonance Imaging: TMRI, vol. 19, no. 6, p. 297, 2008. [PubMed: 19512852]

[6]. Kokes R, Lister K, Gullapalli R, Zhang B, MacMillan A, Richard H, and Desai JP, "Towards a teleoperated needle driver robot with haptic feedback for RFA of breast tumors under continuous MRI," Medical Image Analysis, vol. 13, no. 3, pp. 445–455, 2009. [PubMed: 19303805]

[7]. Seifabadi R, Song SE, Krieger A, Cho NB, Tokuda J, Fichtinger G, and Iordachita I, "Robotic system for MRI-guided prostate biopsy: Feasibility of teleoperated needle insertion and ex vivo phantom study," International Journal of Computer Assisted Radiology and Surgery, vol. 7, no. 2, pp. 181–190, 2012. [PubMed: 21698389]

[8]. Shang W, Su H, Li G, and Fischer GS, "Teleoperation system with hybrid pneumatic-piezoelectric actuation for MRI-guided needle insertion with haptic feedback," in Intelligent Robots and Systems (IROS), 2013 IEEE/RSJ International Conference on. IEEE, 2013, pp. 4092–4098.

[9]. Kim ST, Kim Y, and Kim J, "Design of an MR-compatible biopsy needle manipulator using pull-pull cable transmission," International Journal of Precision Engineering and Manufacturing, vol. 17, no. 9, pp. 1129–1137, 2016.

[10]. Elayaperumal S, Cutkosky MR, Renaud P, and Daniel BL, "A Passive Parallel Master-Slave Mechanism for Magnetic Resonance Imaging-Guided Interventions," Journal of Medical Devices, vol. 9, no. 1, p. 011008, 2015.

[11]. Su H, Shang W, Li G, Patel N, and Fischer GS, "An MRI-Guided Telesurgery System Using a Fabry-Perot Interferometry Force Sensor and a Pneumatic Haptic Device," Annals of Biomedical Engineering, pp. 1–12, 2017.

[12]. Vigaru B, Sulzer J, and Gassert R, "Design and evaluation of a cable-driven fMRI-compatible haptic interface to investigate precision grip control," IEEE Transactions on Haptics, vol. 9, no. 1, pp. 20–32, 2016. [PubMed: 26441454]

[13]. Ho M, McMillan AB, Simard JM, Gullapalli R, and Desai JP, "Toward a meso-scale SMA-actuated MRI-compatible neurosurgical robot," IEEE Transactions on Robotics, vol. 28, no. 1, pp. 213–222, 2012.

[14]. Bae JH, Han AK, Ploch CJ, Daniel BL, and Cutkosky MR, "Haptic feedback of membrane puncture with an mr-compatible instrumented needle and electroactive polymer display," in World Haptics Conference (WHC), 2017 IEEE, 6 2017, pp. 54–59.

[15]. Elayaperumal S, Bae JH, Daniel BL, and Cutkosky MR, “Detection of membrane puncture with haptic feedback using a tip-force sensing needle,” in Intelligent Robots and Systems (IROS), 2014 IEEE/RSJ International Conference on. IEEE, 2014, pp. 3975–3981.

[16]. Bae JH, Ploch CJ, Lin MA, Daniel BL, and Cutkosky MR, “Display of needle tip contact forces for steering guidance,” in Haptics Symposium, 2016 IEEE. IEEE, 2016, pp. 332–337.

[17]. Gerovich O, Marayong P, and Okamura AM, “The effect of visual and haptic feedback on computer-assisted needle insertion,” Computer Aided Surgery, vol. 9, no. 6, pp. 243–249, 2004. [PubMed: 16112974]

[18]. Pacchierotti C, Prattichizzo D, and Kuchenbecker KJ, “Cutaneous feedback of fingertip deformation and vibration for palpation in robotic surgery,” IEEE Transactions on Biomedical Engineering, vol. 63, no. 2, pp. 278–287, 2016. [PubMed: 26186763]

[19]. Talasaz A, Patel RV, and Naish MD, “Haptics-enabled teleoperation for robot-assisted tumor localization,” in Robotics and Automation (ICRA), 2010 IEEE International Conference on. IEEE, 2010, pp. 5340–5345.

[20]. Meli L, Pacchierotti C, and Prattichizzo D, “Experimental evaluation of magnified haptic feedback for robot-assisted needle insertion and palpation,” The International Journal of Medical Robotics and Computer Assisted Surgery, 2017.

[21]. Iordachita I, Sun Z, Balicki M, Kang JU, Phee SJ, Handa J, Gehlbach P, and Taylor R, “A sub-millimetric, 0.25 mN resolution fully integrated fiber-optic force-sensing tool for retinal micro-surgery,” International Journal of Computer Assisted Radiology and Surgery, vol. 4, no. 4, pp. 383–390, 2009. [PubMed: 20033585]

[22]. Monfaredi R, Seifabadi R, Fichtinger G, and Iordachita I, “Design of a decoupled mri-compatible force sensor using fiber bragg grating sensors for robot-assisted prostate interventions,” in SPIE Medical Imaging. International Society for Optics and Photonics, 2013, pp. 867118–867118.

[23]. Elayaperumal S, Bae JH, Christensen D, Cutkosky MR, Daniel BL, Black RJ, Costa JM, Faridian F, and Moslehi B, “MR-compatible biopsy needle with enhanced tip force sensing,” in World Haptics Conference (WHC), 2013 IEEE. IEEE, 2013, pp. 109–114.

[24]. De Lorenzo D, Koseki Y, De Momi E, Chinzei K, and Okamura AM, “Coaxial needle insertion assistant with enhanced force feedback,” IEEE Transactions on Biomedical Engineering, vol. 60, no. 2, pp. 379–389, 2013. [PubMed: 23193302]

[25]. Beekmans S, Lembrechts T, van den Dobbelsteen J, and van Gerwen D, “Fiber-Optic Fabry-Pérot Interferometers for Axial Force Sensing on the Tip of a Needle,” Sensors, vol. 17, no. 1, p. 38, 2016.

[26]. Tse ZTH, Elhawary H, Rea M, Davies B, Young I, and Lamperth M, “Haptic needle unit for MR-guided biopsy and its control,” IEEE/ASME Transactions on Mechatronics, vol. 17, no. 1, pp. 183–187, 2012.

[27]. Ergin MA, Kuhne M, Thielscher A, and Peer A, “Design of a new MR-compatible haptic interface with six actuated degrees of freedom,” in Biomedical Robotics and Biomechatronics IEEE RAS/EMBS International Conference on, 2014, pp. 293–300.

[28]. Erwin A, O’Malley M, Ress D, and Sergi F, “Kinesthetic feedback during 2dof wrist movements via a novel mr-compatible robot,” IEEE Transactions on Neural Systems and Rehabilitation Engineering, 2016.

[29]. Hara M, Matthey G, and Yamamoto A, “Development of a 2-DOF Electrostatic Haptic Joystick for MRI/fMRI Applications,” in Robotics and Automation (ICRA), 2009 IEEE International Conference on, 2009, pp. 1479–1484.

[30]. Yu N, Hollnagel C, Blickenstorfer A, Kollias SS, and Riener R, “Comparison of MRI-Compatible Mechatronic Systems With Hydrodynamic and Pneumatic Actuation,” Transactions on Mechatronics, vol. 13, no. 3, pp. 268–277, 2008.

[31]. Shang W, Su H, Li G, and Fischer GS, “Teleoperation system with hybrid pneumatic-piezoelectric actuation for MRI-guided needle insertion with haptic feedback,” in Intelligent Robots and Systems (IROS), 2013 IEEE/RSJ International Conference on, 2013, pp. 4092–4098.

[32]. Gassert R, Yamamoto A, Chapuis D, Dovat L, Bleuler H, and Burdet E, “Actuation methods for applications in mr environments,” Concepts in Magnetic Resonance Part B: Magnetic Resonance Engineering, vol. 29B, no. 4, pp. 191–209, 2006.

[33]. Tsekos NV, Khanicheh A, Christoforou E, and Mavroidis C, “Magnetic resonance compatible robotic and mechatronics systems for image-guided interventions and rehabilitation : A review study,” Annual Review of Biomedical Engineering, pp. 351–389, 2007.

[34]. Chakraborti P, Toprakci HAK, Yang P, Di Spigna N, Franzon P, and Ghosh T, “A compact dielectric elastomer tubular actuator for refreshable Braille displays,” Sensors and Actuators, A: Physical, vol. 179, pp. 151–157, 2012.

[35]. Mazzone A, Zhang R, and Kunz A, “Novel actuators for haptic displays based on electroactive polymers,” in Proceedings of the ACM Symposium on Virtual Reality Software and Technology. ACM, 2003, pp. 196–204.

[36]. Vogan J, Wingert A, Dubowsky S, Hafez M, Kacher D, and Jolesz F, “Manipulation in MRI devices using electrostrictive polymer actuators: With an application to reconfigurable imaging coils,” in Robotics and Automation (ICRA), 2004 IEEE International Conference on, 2004, pp. 2498–2504.

[37]. Plante J-S, Tadakuma K, DeVita L, Kacher D, Roebuck J, DiMaio S, Jolesz F, and Dubowsky S, “An MRI-compatible needle manipulator concept based on elastically averaged dielectric elastomer actuators for prostate cancer treatment: an accuracy and MR-compatibility evaluation in phantoms,” Journal of Medical Devices, vol. 3, no. 3, p. 031005 (10 pp.), 2009.

[38]. Carpi F, Khanicheh A, Mavroidis C, and De Rossi D, “Silicone made contractile dielectric elastomer actuators inside 3-Tesla MRI environment,” in Intelligent Robots and Systems (IROS), 2008 IEEE/RSJ International Conference on, 2008, pp. 137–142.

[39]. Gleeson BT, Horschel SK, and Provancher WR, “Design of a fingertip-mounted tactile display with tangential skin displacement feedback,” IEEE Transactions on Haptics, vol. 3, no. 4, pp. 297–301, 2010. [PubMed: 27780150]

[40]. Ploch CJ, Bae JH, Ju W, and Cutkosky M, “Haptic skin stretch on a steering wheel for displaying preview information in autonomous cars,” in Intelligent Robots and Systems (IROS), 2016 IEEE/RSJ International Conference on. IEEE, 2016, pp. 60–65.

[41]. Quek ZF, Schorr SB, Nisky I, Provancher WR, and Oka-mura AM, “Sensory substitution and augmentation using 3-degree-of- freedom skin deformation feedback,” IEEE Transactions on Haptics, vol. 8, no. 2, pp. 209–221, 2015. [PubMed: 25647582]

[42]. Leonardis D, Solazzi M, Bortone I, and Frisoli A, “A 3-rsr haptic wearable device for rendering fingertip contact forces,” IEEE Transactions on Haptics, 2016.

[43]. Girard A, Marchal M, Gosselin F, Chabrier A, Louveau F, and Lécuyer A, “Haptip: Displaying haptic shear forces at the fingertips for multi-finger interaction in virtual environments,” Frontiers in ICT, vol. 3, p. 6, 2016.

[44]. Pelrine R, Kornbluh R, Joseph J, Heydt R, Pei Q, and Chiba S, “High-field deformation of elastomeric dielectrics for actuators,” Materials Science and Engineering C, vol. 11, no. 2, pp. 89–100, 2000.

[45]. Orita A and Cutkosky MR, “Scalable electroactive polymer for variable stiffness suspensions,” IEEE/ASME Transactions on Mechatronics, vol. 21, no. 6, pp. 2836–2846, 2016.

[46]. Gleeson BT, Stewart CA, and Provancher WR, “Improved tactile shear feedback: Tactor design and an aperture-based restraint,” IEEE Transactions on Haptics, vol. 4, no. 4, pp. 253–262, 2011. [PubMed: 26963654]

[47]. Nakazawa N, Ikeura R, and Inooka H, “Characteristics of human fingertips in the shearing direction.” Biological Cybernetics, vol. 82, no. 3, pp. 207–14, 2000. [PubMed: 10664107]

[48]. Mueller S and Sandrin L, “Liver stiffness: a novel parameter for the diagnosis of liver disease,” Hepatic Medicine: Evidence and Research, vol. 2, p. 49, 2010. [PubMed: 24367208]

[49]. Elayaperumal S, Bae JH, Daniel BL, and Cutkosky MR, “Detection of membrane puncture with haptic feedback using a tip-force sensing needle,” in Intelligent Robots and Systems (IROS), 2014 IEEE/RSJ International Conference on, 2014, pp. 3975–3981.

[50]. Levitt H, “Transformed up- down methods in psychoacoustics,” pp. 467–477,1971.

[51]. Hauthal N, Debener S, Rach S, Sandmann P, and Thorne JD, “Visuo-tactile interactions in the congenitally deaf: a behavioral and event-related potential study,” Frontiers in Integrative Neuroscience, vol. 8, 2014.

[52]. Hecht D, Reiner M, and Karni A, “Enhancement of response times to bi-and tri-modal sensory stimuli during active movements,” Experimental Brain Research, vol. 185, no. 4, p. 655, 2008. [PubMed: 17992522]

[53]. Heverly M, Dupont P, and Triedman J, “Trajectory optimization for dynamic needle insertion,” in Robotics and Automation (ICRA), 2005 IEEE International Conference on. IEEE, 2005, pp. 1646–1651.

[54]. Johansson RS, “Skin mechanoreceptors in the human hand: receptive field characteristics,” Sensory Functions of the Skin in Primates, vol. 27, 1976.

[55]. Bark K, Wheeler JW, Premakumar S, and Cutkosky MR, “Comparison of skin stretch and vibrotactile stimulation for feedback of proprioceptive information,” Haptic Interfaces for Virtual Environment and Teleoperator Systems, 2008 Symposium on, pp. 71–78, 2008.

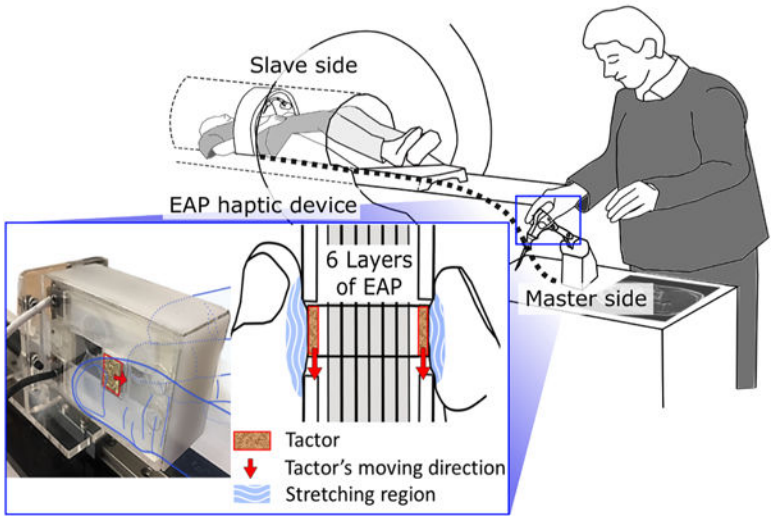

Fig. 1.

A haptic display can relay tool tip forces to a physician performing MR-guided procedures. Inset: detail of display held between thumb and index finger.

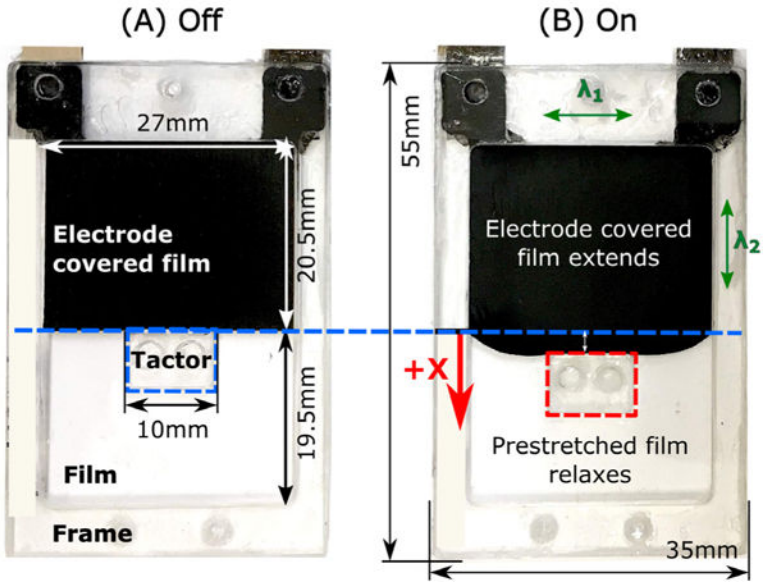

Fig. 2.

EAP before (A) and after (B) applying 5.75 kV, which causes the film between the black electrodes to expand, producing motion in the *x* direction up to 2.5 mm (13% of the length of the electrodes). The film prestretch directions are depicted as λ_1 and λ_2.

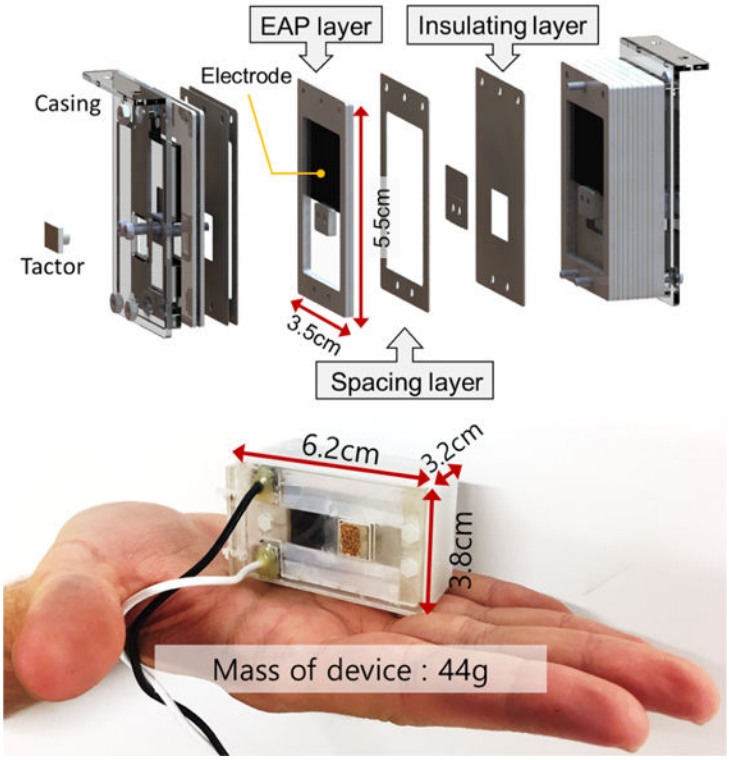

Fig.3.

Exploded view of the haptic device showing dimensions compared to a hand. Six layers of EAP actuators are stacked to power the device. Insulating layers prevent arcing and spacing layers facilitate smooth tactor movement by preventing friction.

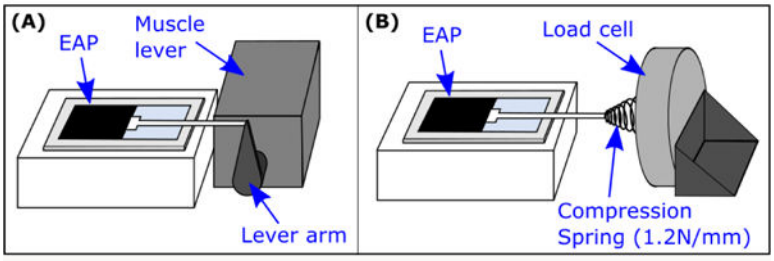

Fig. 4.

Testing apparatus. (A) EAP actuator is connected to a muscle lever for force and displacement measurements. (B) EAP is connected to a compression coil spring and a load cell for predicting the behavior when pressed against a human fingerpad.

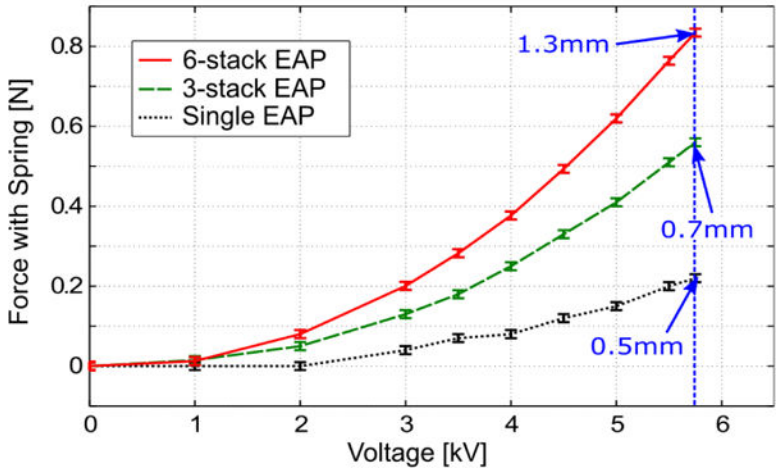

Fig. 5.

Characterization of EAPs with a spring in series. The displacement noted for each case at 5.75 kV is the maximum displacement when connected to a spring.

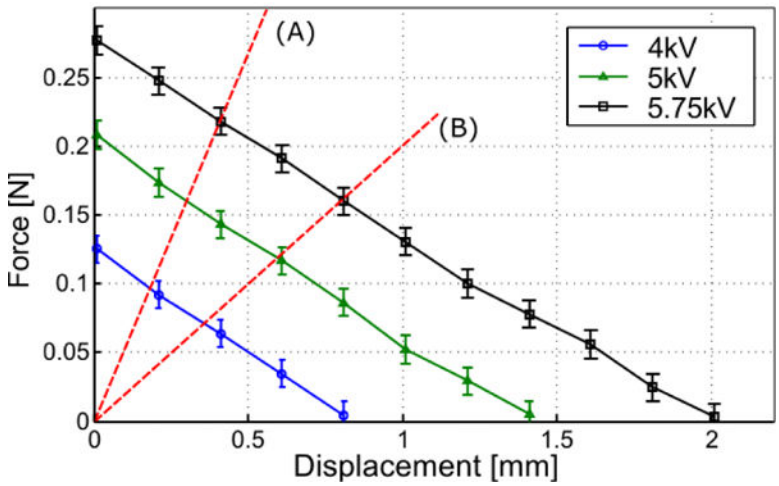

Fig. 6.

Force-displacement relationships of a single EAP for different voltages represented by solid lines. Dashed lines (A) and (B) represent two different human fingerpad stiffnesses. The force and displacement experienced by a fingerpad of stiffness (A) or (B) is equal to the coordinates of the intersection point with the line of that stiffness and the force-displacement line of the correct voltage.

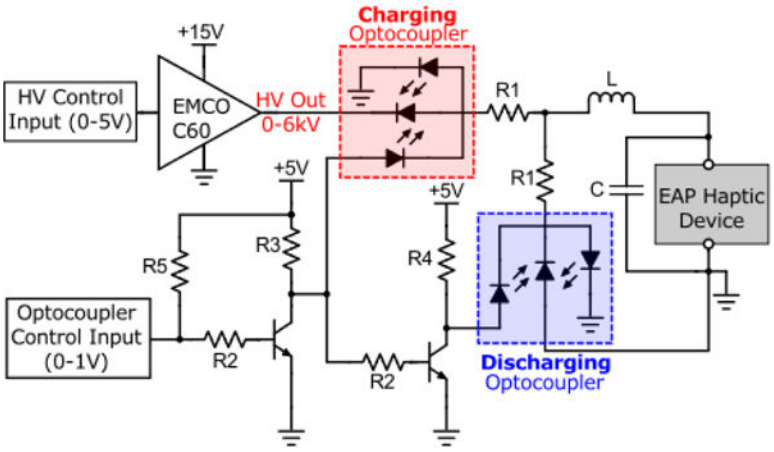

Fig. 7.
Modified miniature HV circuit for usage in MR room.

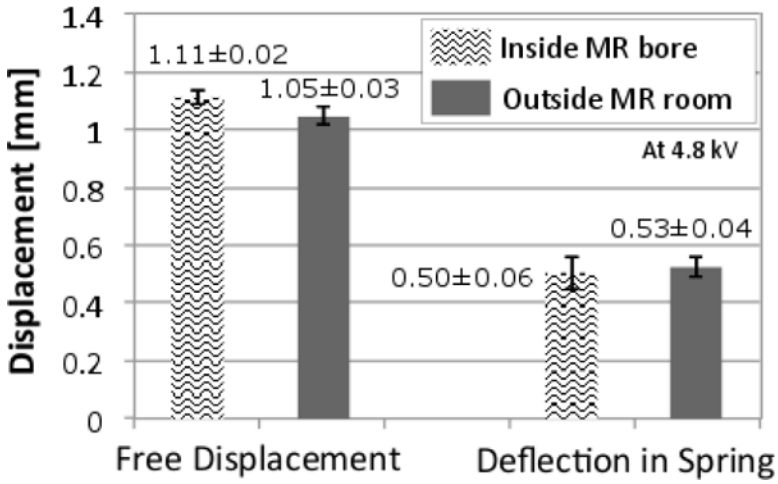

Fig. 8.

Effect of 3 T magnetic field on the performance of the EAP haptic device. Three data points are collected for each condition using video recordings.

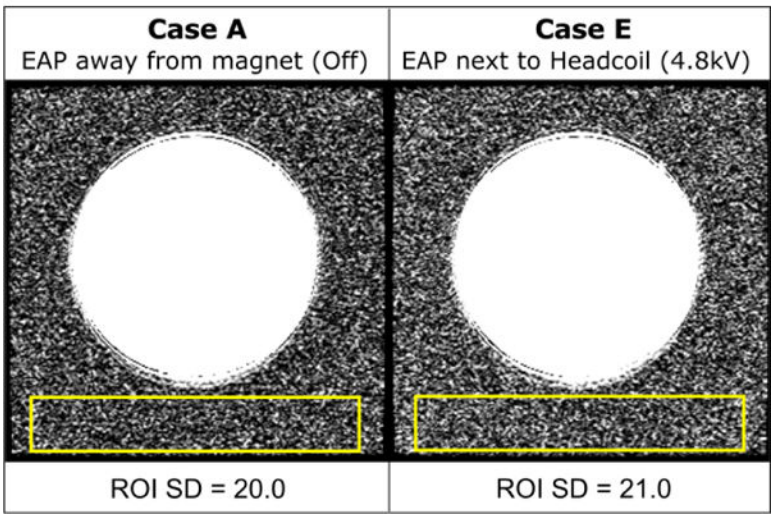

Fig. 9.

Comparing anatomic images with 0 V and a 4.8 kV square wave. The yellow boxes indicate the regions of interest (ROI).

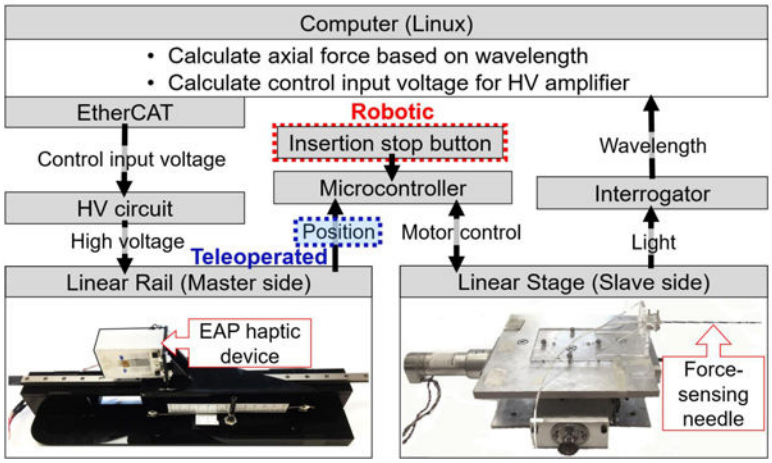

Fig. 10.

System schematic block diagram for both robotic and teleoperated membrane puncture test setups. The robotic insertion case has a button to stop the insertion. While the linear stage automatically inserts the needle with constant speed (6mm/s), in the teleoperated case the user manually controls the insertion speed.

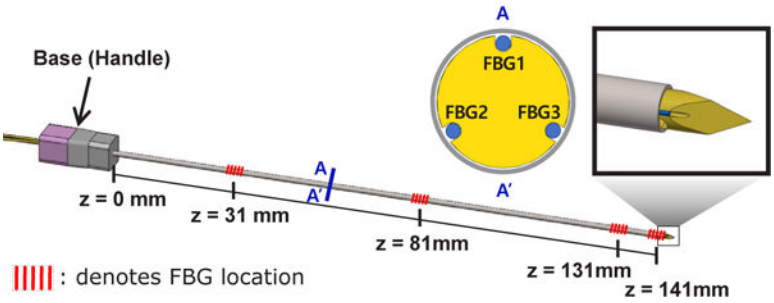

Fig.11.
Configuration of the force-sensing needle and sensor locations.

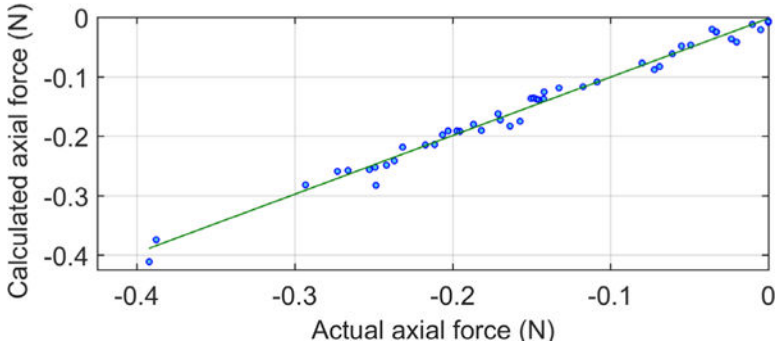

Fig. 12.

Axial force calibration result of the force-sensing needle. The calculated axial force is linearly proportional to the actual axial force applied on the needle tip.

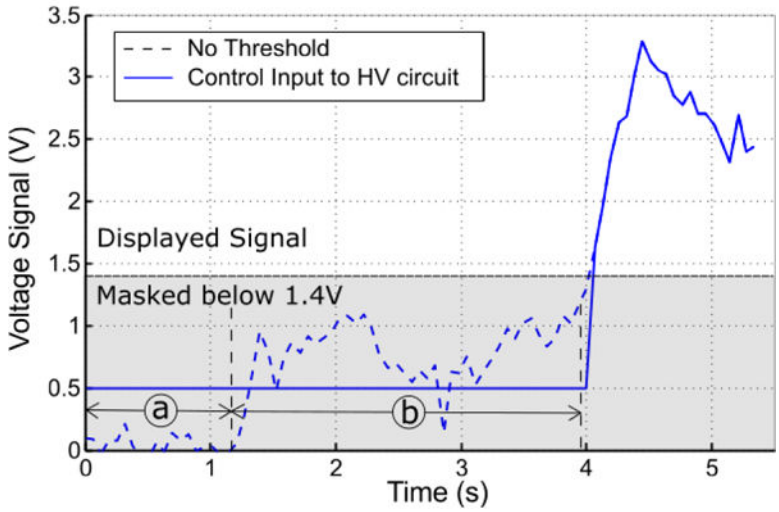

Fig. 13.

Amplified input voltage with and without threshold. The threshold (1.4V) was set to avoid low-level noise. In part (a) of the no-threshold plot, the needle did not move. From 1.2 sec to 4 sec, region (b), the needle was cutting through a gelatin phantom and the force graph shows the resistance force from the gelatin tissue. If the commanded input voltage is below 1.4 V, it is set to 0.5 V with the threshold. The input voltage is also capped at 3.3 V to prolong EAP life.

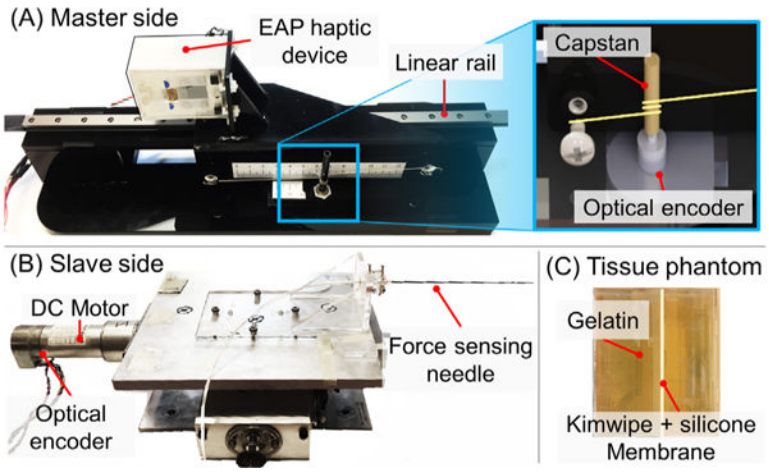

Fig. 14.

Teleoperation system configuration. (A) Master side: The EAP haptic device was mounted on the linear rail's cart. The position of the cart was measured by an optical encoder attached to a capstan. (B) Slave side: A DC motor drives the slave side (linear stage) based on the position of the master. (C) Tissue phantom: tissue phantom was made with gelatin and kimwipe + silicone membrane.

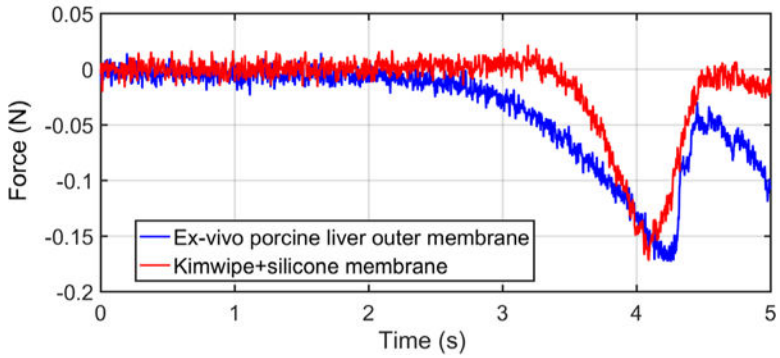

Fig. 15.

Membrane puncture force comparison for phantom and ex-vivo porcine liver. Both have a similar peak amplitude of 0.17 N.

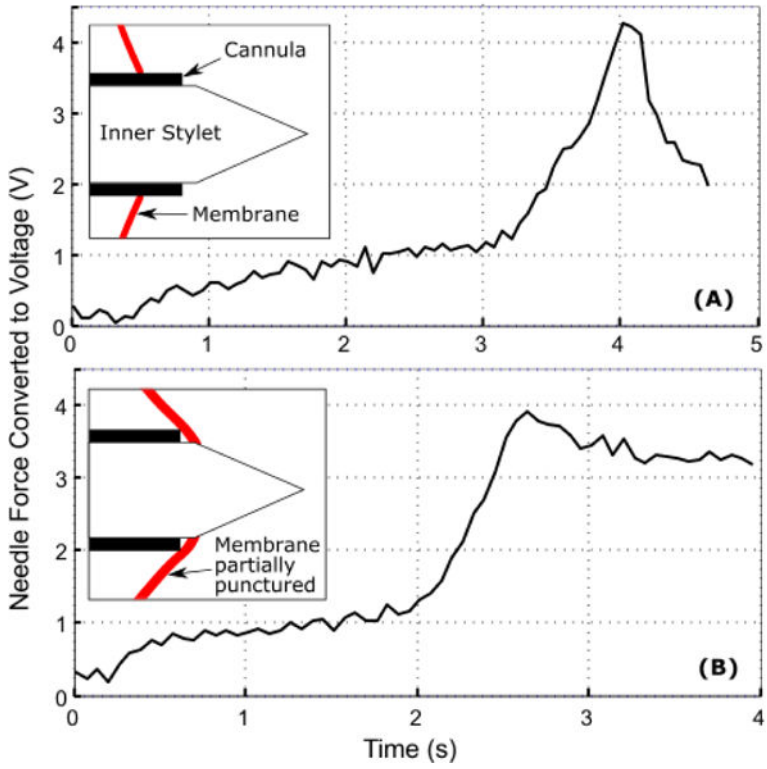

Fig. 16.

Two types of membrane punctures: (A) membrane is thoroughly punctured (B) only the inner stylet punctured the membrane and the membrane is stuck on the outer cannula.

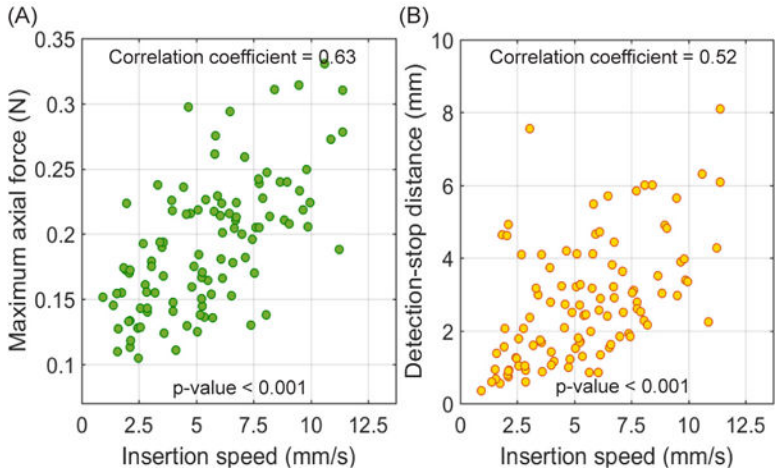

Fig. 17.

(A) Correlations between insertion speed and maximum axial force during membrane puncture. (B) Correlations between insertion speed and the detection distance.

TABLE 1:

tSNR Values for Test Conditions A-E

Case	HV Circuit	Voltage Across EAP	Distance of EAP from Iso-center	tSNR	tSNR Reduction Relative to:	
					Case A	Case C
A	Off	0	Outside of magnet (3 m)	472		
B	Off	0	Next to head coil (14 cm)	465	1.48 %	
C	On	0		464	1.69 %	
D	On	3 kV		464	1.69 %	0%
E	On	4.8 kV		462	2.12 %	0.43 %

TABLE 2:

Threshold of Perceptible Force Results for 12 Subjects. Reported force values can be converted to displacements using finger pad stiffness.

Force	0.25 N/s	0.52 N/s	1.06 N/s
Mean (N)	0.13	0.11	0.07
SD (N)	0.02	0.01	0.01
[39] stretching finger pad	0.5 mm/s	1 mm/s	
	~0.05 mm	less than 0.05 mm	
[40] stretching palm	1 mm/s	2 mm/s	
	0.44 mm	0.26 mm	

TABLE 3:

Results of Teleoperated Membrane Detection Test

	Insertion Speed (mm/s)	Tip-membrane ddedeistance after puncture (mm)	Detect-stop distance (mm)
Mean	5.46	0.34	2.78
SD	2.65	0.46	1.66
Min	0.93	0.00	0.36
Max	11.38	2.89	8.10

	Peak axial Force (N)	Peak EAP force (N)	Peak V control input to HV amplifier (V)	V control input slope (V/s)
Mean	0.19	0.49	2.89	4.14
SD	0.05	0.23	0.87	2.39
Min	0.10	0.10	1.44	0.16
Max	0.33	1.11	5.18	15.50